Science and Technology Indonesia
e-ISSN:2580-4391 *p*-ISSN:2580-4405
Vol. 11, No. 3, July 2026

Research Paper

Engineering the Anatase-Rutile Phase Composition of TiO_2 through H_2O_2 Addition and Its Photocatalytic Activity

Sri Wahyuni[1*], Sri Kadarwati[1], M. Alauhdin[1], Addy Rachmat[2], Nuril Huda[1], Eka Siti Rinjani[1], Ridho Prasetyo[1,3]

[1]*Chemistry Study Programme, the Faculty of Mathematics and Natural Sciences, Universitas Negeri Semarang, Semarang, Central Java, 50229, Indonesia*
[2]*Department of Chemistry, Faculty of Mathematics and Natural Sciences, Universitas Sriwijaya, Ogan Ilir, South Sumatra, 30662, Indonesia*
[3]*Departement of Chemical Engineering, Universitas Diponegoro, Semarang, Central Java, 50275, Indonesia*
***Corresponding author**: sriwahyunikimia@mail.unnes.ac.id

Abstract
The synthesis of mixed-phase anatase-rutile TiO_2 has been carried out to improve its light response and photocatalytic activity. The synthesis of mixed-phase TiO_2 was performed through a sol–gel method in an alkaline solution and followed by a hydrothermal process in an autoclave at a temperature of 150 °C for 3 h. A 60 mL of 0.5 M HNO_3 then was added into the TiO_2 precipitate followed by the addition of various amount (0 mL, 10 mL, and 20 mL) of H_2O_2 30%. The suspension was homogenized by a sonication for 30 min to obtain an anatase-rutile mixture phase. The resulted mixed-phase TiO_2 was further labelled as A_0, A_1, and A_2, respectively. The High-Score analysis showed that the phase composition of TiO_2 was 9.4% anatase, 90.6% rutile (A_0); 17% anatase, 83% rutile (A_1); and 49.6% anatase, 50.4% rutile (A_2). The spectra of diffuse-reflectance showed a shift in the band gap energy from 3.17 eV (fully anatase) TiO_2 to 2.75-2.86 eV in A_0, A_1, and A_2 mixed-phase TiO_2. These results suggested that the photocatalytic activity of A_1 and A_2 mixed-phase TiO_2 would take place in the early visible-light region ($\lambda > 400$ nm). The photocatalytic examination of the mixed-phase TiO_2 under LED and UV irradiation resulted in a decrease in the rhodamine-B (Rh-B) concentration of up to 92%. However, the photocatalytic activity of mixed-phase TiO_2 did not outperform that of the fully anatase TiO_2, achieving 98% reduction in Rh-B concentration.

Keywords
Mixed-Phase TiO_2, Sol-Gel, Hydrothermal, Anatase-Rutile, SDGs 6, Wastewater Treatment

Received: 27 February 2026, Accepted: 30 April 2026
https://doi.org/10.26554/sti.2026.11.3.955-971

1. INTRODUCTION

Titanium dioxide (TiO_2), also known as titania, is widely regarded as one of the most effective and versatile semiconductor photocatalysts. Its exceptional physicochemical stability, low toxicity, and strong oxidizing capability have driven extensive research into applications such as environmental remediation (Lazar et al., 2012; Wahyuni et al., 2018), photocatalytic water splitting for hydrogen production, air purification, self-cleaning surfaces, sensing materials, and antibacterial coatings (Mardiana et al., 2026; Pelaez et al., 2012; Wahyuni et al., 2024). TiO_2 primarily exists in three crystalline polymorphs-anatase, rutile, and brookite-with anatase and rutile being the most prevalent. Anatase exhibits a bandgap of approximately 3.2 eV, whereas rutile has a slightly narrower bandgap of ~3.0 eV. Despite its advantageous properties, this wide bandgap restricts the photoexcitation to the ultraviolet (UV) region, which constitutes only ~4-5% of the solar spectrum, thereby limiting its practical efficiency under visible or solar light irradiation.

To overcome these intrinsic limitations, various modification strategies have been explored, including metal/non-metal doping and fabrication of heterojunction composites such as TiO_2/CuO (Mandari et al., 2017), TiO_2/polyaniline (Rokade et al., 2024), and TiO_2/SiO_2 (Wahyuni et al., 2024). Among these approaches, phase engineering, specifically the controlled formation of a mixed anatase-rutile structure, has emerged as a particularly promising route to enhance its photocatalytic performance. The staggered band alignment at the anatase-rutile interface would promote a spatial charge separation, so that significantly suppressing the electron-hole recombination (Lei et al., 2021). Furthermore, the mixed-phase TiO_2 exhibited an extended optical response range and often possessed a higher specific surface area with abundant surface defects and active sites, which collectively enhanced the reactant adsorption and catalytic turnover (Eddy et al., 2023; Wang et al., 2020). Consequently, the precise regulation of the anatase-to-rutile (A/R) phase ratio has been considered as a critical strategy for optimizing its photocatalytic efficiency.

The sol-gel method remained widely adopted for the mixed-phase TiO_2 synthesis due to its simplicity, low processing temperature, and excellent compositional control (Bokov et al., 2021). Within this framework, the A/R ratio could be effectively modulated by adjusting chemical additives and reaction parameters. For an instance, Cheng et al. (2014) demonstrated that the concentration of HNO_3 solution could regulate the phase composition, while Wang et al. (2020) achieved a finer control by employing a combination of HNO_3 and H_2O_2.

The role of H_2O_2 in regulating the phase composition of TiO_2 has been reported in several studies, particularly during the synthesis under hydrothermal conditions. The presence of H_2O_2 would enable the controlled tuning of the anatase-rutile ratio through oxidative and complexation effects on titanium precursors (Spada et al., 2017; Yaemsunthorn et al., 2021). These previous studies mainly emphasized its function during the precursor transformation rather than after hydrothermal treatment. In terms of phase transformation, the anatase-to-rutile transition was generally governed by dissolution- precipitation and interface-nucleation mechanisms, which would be influenced by pH and temperature and might be indirectly affected by the presence of H_2O_2 (Sabyrov and Penn, 2016).

Beyond conventional sol- gel processing, emerging approaches such as the polyol-solid surface/interface transesterification method have recently enabled a highly precise A/R ratio modulation in TiO_2 nanostructures (Zhang et al., 2015). Additionally, thermal and environmental conditions played a decisive role in the phase evolution; acidic sol-gel environments and moderate calcination temperatures tended to stabilize the anatase phase, whereas elevated temperatures and prolonged reaction times would promote the rutile crystallization (Jacob et al., 2022; Rokade et al., 2024). However, many existing protocols still relied on the extended hydrothermal/solvothermal durations (up to 24 h) or high-energy calcination steps, which compromised the scalability, energy efficiency, and cost-effectiveness.

Although the influence of HNO_3 concentration and calcination parameters on the anatase-to-rutile phase transition has been well documented (Cheng et al., 2014), the potential of hydrogen peroxide (H_2O_2) as a post-hydrothermal additive for a precise phase engineering remains underexplored. Moreover, conventional synthesis routes often involved time-intensive procedures that hindered a large-scale catalyst production. To address these limitations, this study introduced a simplified, time-efficient synthesis strategy that utilized a controlled post-hydrothermal by H_2O_2 addition to tailor the anatase–rutile phase ratio. This study systematically investigated the effect of the addition of H_2O_2 in different volumes (0, 10, and 20 mL) on the crystallinity, band gap energy, surface morphology, and visible-light photocatalytic activity of the resulted TiO_2. By optimizing this streamlined approach, the development of a scalable, energy-efficient pathway to engineer high-performance mixed-phase TiO_2 photocatalysts, ultimately advancing their applicability in sustainable environmental and energy technologies was targeted.

2. EXPERIMENTAL SECTION

2.1 Materials

All chemical reagents were of an analytical grade and used without further purification. Titanium (IV) tetraisopropoxide (TTIP, ≥97%, Sigma-Aldrich, Germany) was used as the titanium precursor. Sodium ethylenediaminetetraacetate (Na_2 EDTA-$2H_2O$), ammonia solution (25%), sodium hydroxide (NaOH, 99%), nitric acid (HNO_3 65%), and hydrogen peroxide (H_2O_2, 30%) were obtained from Merck, Germany. Rhodamine-B (Rh-B) (Merck, Germany) was used as the model pollutant for the photocatalytic evaluation. Distilled water was used throughout the experiments.

2.2 Instruments and Characterization Methods

- **Crystallinity and Phase Analysis:** The powder X-ray diffraction (XRD) patterns were recorded using a Panalytical X'Pert^3 diffractometer with a Cu-Kα radiation (λ = 0.15406 nm) at 40 kV and 30 mA. The phase composition and crystallite size were determined using High-Score Plus software and the Debye–Scherrer equation, respectively.
- **Optical Properties:** The diffuse reflectance UV-Vis spectra were obtained using a Shimadzu UV-Vis (double beam/single beam) spectrophotometer. The band gap energy of the synthesized mixed-phase TiO_2 was determined via the Tauc plot method (Kubelka–Munk function).
- **Surface Area and Porosity:** Nitrogen adsorption- desorption isotherms were measured at 77 K using a Quantachrome BET analyzer instrument of 11.0 version. The specific surface area of the synthesized mixed-phase TiO_2 was calculated using the BET method, while pore size distribution was analyzed via the BJH desorption model.
- **Morphological Analysis:** The surface morphology of the synthesized mixed-phase TiO_2 was examined using a Phenom Pro X Desktop scanning electron microscope equipped with an EDS and a Talos F200X transmission electron microscope.

2.3 Synthesis Procedure of Mixed-Phase Anatase-Rutile TiO_2

The mixed-phase anatase-rutile TiO_2 was synthesized via a modified sol-gel and hydrothermal route based on previous reports (Cheng et al., 2014; Christy et al., 2010). The procedure is summarized as follows:

1. **Gel Formation:** A 5 mmol of Na_2EDTA was dissolved in 15 mL of distilled water. The pH of the solution was adjusted to 9-10 using 25% ammonia solution. Subsequently, a 5 mL of TTIP (~16.9 mmol) was added dropwise to the alkaline EDTA solution under a continuous magnetic stirring for 30 min to ensure a complete hydrolysis. The resulted suspension was further homogenized using an ultrasonic irradiation for another 30 min.
2. **Hydrothermal Treatment:** The gel suspension was mixed with 60 mL of 1 M NaOH to obtain a strongly alkaline

hydrothermal medium (pH >13), then transferred to a Teflon-lined stainless-steel autoclave (100 mL capacity). The hydrothermal reaction was carried out at 150°C for 3 h. It is important to note that no HNO_3 or H_2O_2 was added during this hydrothermal step. After natural cooling to room temperature, the white precipitate was collected by centrifugation and washed repeatedly using distilled water until the supernatant was neutral (pH of ~7) to remove residual sodium ions and alkali.

3. **Post-Hydrothermal Acid Treatment and Phase Regulation:** The washed solid was dispersed in 60 mL of 0.5 M HNO_3 (added after hydrothermal treatment) and stirred at 70°C for 60 min to facilitate the proton exchange and phase transformation. The suspension was then sonicated for 30 min to ensure its homogeneity. Subsequently, H_2O_2 with various volumes (0, 10, or 20 mL) were added as a peptizing agent to the acidified suspension to regulate the anatase-rutile phase ratio. The mixture was further sonicated for 30 min to achieve a uniform dispersion.
4. **Drying and Calcination:** The resulted precipitate was recovered by centrifugation, dried at 100°C for 3 h, and subsequently calcined at 400°C for 2 h in air with a heating rate of 5°C/min. The final products were labelled as A_0, A_1, and A_2, corresponding to the addition of 0, 10, and 20 mL of H_2O_2, respectively.

2.4 Photocatalytic Testing Procedure

The photocatalytic activity of the synthesized TiO_2 samples was evaluated through the degradation of rhodamine-B (Rh-B) under an LED-UV irradiation. Rhodamine-B is commonly found in water bodies contaminated with textile waste (Fitri et al., 2024).

1. **Adsorption–Desorption Equilibrium:** A 100 mg of photocatalysts (fully anatase TiO_2, and A0, A1 and A2 mixed-phase TiO_2) was dispersed in 100 mL of 25 ppm Rh-B solution and stirred in the dark for 30 min to achieve an adsorption–desorption equilibrium.
2. **Photocatalytic Activity:** The photocatalytic activity was evaluated under a combined LED-UV irradiation system. A 100 W white LED lamp (serving as the visible-light source) and a 40 W UV lamp (λ_{max} = 365 nm) were used as the light sources. Both lamps were mounted 15 cm above the center of the cylindrical glass reactor (100 mL capacity) containing the catalyst suspension. The reaction mixture was continuously stirred to ensure a homogeneous exposure to light. Although absolute irradiance values were not quantified in this study, the fixed geometry and lamp specifications were maintained consistently across all experiments to ensure the comparability of the photocatalytic results.
3. **Quantification:** The residual Rh-B concentration was measured using a UV-Vis spectrophotometer at its maximum absorption wavelength (λ_{max} = 554 nm). The degradation efficiency (%) was calculated using Equation (1), where C_0 and C_t are the initial and time-dependent concentrations of Rh-B, respectively.

$$\text{Degradation (\%)} = \left(\frac{C_t}{C_0}\right) \times 100 \quad (1)$$

4. **Reusability Test:** The used catalyst was recovered by centrifugation, washed with distilled water, dried, and reused for two additional cycles under identical conditions to evaluate its stability.

2.5 Data Analysis and Calculations

- **Crystallite Size:** The crystallite size of the synthesized TiO_2 was calculated using the Debye–Scherrer equation (Equation (2)), where D is crystallite size, K is Scherrer constant (0.9), λ is X-ray wavelength (0.15406 nm), β is full width at half maximum (FWHM), and θ is Bragg angle.

$$D = \frac{K\lambda}{\beta \cos\theta} \quad (2)$$

- **Phase Composition:** The phase composition of the mixed-phase TiO_2 was determined using the Reference Intensity Ratio (RIR) method in High-Score Plus software based on the XRD peak intensities of anatase (JCPDS 01-086-1157) and rutile (JCPDS 01-076-0324).
- **Band Gap Energy:** The band gap energy of the mixed-phase TiO_2 was estimated from diffuse reflectance data using the Tauc plot relation in Equation (3), where $n = 2$ for indirect transition (anatase/rutile TiO_2).

$$[F(R) \cdot h\nu]^{1/n} = B(h\nu - E_g) \quad (3)$$

3. RESULTS AND DISCUSSION

3.1 The Crystallinity and Phase Composition of TiO_2

Figure 1 shows the XRD patterns of the fully anatase TiO_2 and the mixed-phase anatase-rutile TiO_2 (A_0, A_1, and A_2). The XRD patterns showed the anatase (A) and rutile (R) phases, as confirmed by matching them with the JCPDS databases 01-086-1157 (anatase) and 01-076-0324 (rutile). The analysis and graphing of the XRD patterns were performed using High-Score Plus and Origin Pro software, respectively. The XRD pattern of fully anatase TiO_2 showed a 100% anatase phase, with a tetragonal crystal system. No rutile phase was observed in the pattern. The peaks identified as the anatase phase were those at 2θ of 25.22° (101), 37.84° (004), 47.92° (200), 53.98° (105), 55.00° (211), 62.54° (204), 68.70° (116), 70.18° (220), and 75.24° (215).

In the case of the mixed-phase TiO_2, anatase and rutile phases were observed. The XRD pattern of A_0 TiO_2 showed the composition of the anatase and rutile phases with a ratio of 9.4% anatase to 89.6% rutile. The XRD pattern of

A1 TiO_2 showed a phase composition of 17% anatase and 83% rutile. The mixed-phase TiO_2 was identified as tetragonal. The peaks identified as the rutile phase were those at 2θ of 27.22° (110), 36.16° (101), 41.12° (111), 43.56° (210), 54.16° (211), 56.35° (220), and 68.62° (112). While the anatase phase was identified at peaks with 2θ of 37.80° (004), 54.16° (105), 62.88° (204), 68.62° (116), and 70.02° (220). The XRD pattern of the A2 TiO_2 showed the composition of the anatase and rutile phases of 49.8% anatase and 50.2% rutile. The peaks identified as the rutile phase were those at 2θ of 27.36° (110), 36.06° (101), 41.34° (111), 44.90° (210), 54.56° (211), 56.20° (220), 62.96° (310), and 69.62° (112). While the anatase phase was identified at peaks with 2θ of 25.44° (101), 37.66° (004), 47.98° (200), 62.96° (204), 69.62° (116), and 75.60° (215). The peaks that appeared on the XRD patterns were in accordance with the previously reported by El-Desoky et al. (2020) where the highest peaks of the identified rutile and anatase phases were shown in the grid planes (110) and (101).

To compare the characteristics of the synthesized mixed-phase TiO_2, a crystallite size calculation was performed using the Debye-Scherrer equation (Equation (2)). The obtained crystallite sizes of fully anatase TiO_2 and mixed-phase TiO_2 (A_0, A_1, and A_2) were 14.053 nm, 10.382 nm, 11.252 nm, and 12.611 nm, respectively, as listed in Table 1. The fully anatase TiO_2 had the largest crystallite size compared to the A0, A1, and A2 mixed phases. In addition, the crystal lattice was also analyzed using the High-Score Plus software, yielding the lattice parameters. The volume cells of anatase from the fully anatase TiO_2, A_0, A_1, and A_2 mixed phases were 136.43 $Å^3$, 136.17 $Å^3$, 137.29 $Å^3$, 135.11 $Å^3$ while those of rutile from the fully anatase TiO_2, A0, A1, and A2 were 0 $Å^3$, 63.010 $Å^3$, 62.57 $Å^3$, and 61.60 $Å^3$, respectively. In the case of crystal structures, a smaller lattice volume was usually related to a closer distance between atoms. This could lead to a wider band gap requiring a more energy for electron excitation. As a result, this would affect the photocatalytic activity of the materials, that would relate to the ability of materials to use the photon energy to catalyze chemical reactions. On the other hand, a narrower band gap was usually found in lattices with a greater spacing between atoms. This would facilitate the excitation of electrons with longer wavelengths of light, which would be beneficial for photocatalytic applications (Ahmed et al., 2025).

The crystallinity of fully anatase TiO_2, and A_0, A_1, and A_2 mixed phases was 72.181%, 63.689%, 57.159%, and 52.161%, respectively. The change in the crystallinity was affected by the volume of the cell in the material. An increase in the lattice volume would provide a more space between atoms, which would promote a decrease in the crystallinity (Ahmed et al., 2025). This was because the extra space disrupted the orderly arrangement of atoms. This statement was relevant to the crystallinity calculation results: the anatase composition of the A_2 mixed phase (49.8%) was higher than that of A_1 (17%), resulting in a lower crystallinity for A_2 (52.161%) than that for A_1 (57.159%). Conversely, a reduction in the lattice volume could increase the crystallinity by encouraging atoms to be more densely arranged in the lattices relevant to crystallinity. This was relevant to the crystallinity of the A_0 mixed phase, with a grid crystal composition dominated by the rutile phase of 89.6% (smaller lattice volume), resulting in a higher crystallinity (63.689%) when compared to the other two mixed phases, i.e., A_1 and A_2 (57.159% and 52.161%, respectively).

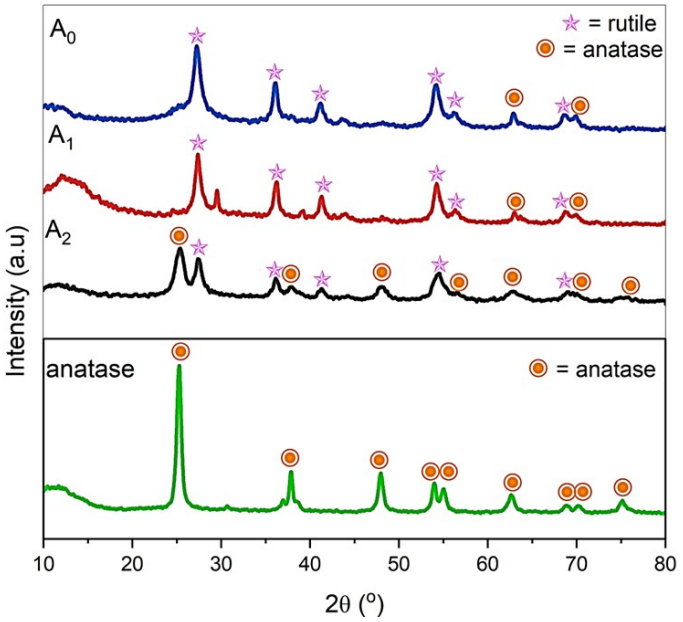

Figure 1. The XRD Patterns of the Fully Anatase TiO_2, and the A_0, A_1, dan A_2 mixed-phase TiO_2

Table 1. The Crystallinity and Crystallite Size of the Fully Anatase and Mixed-Phase TiO_2

Sample	Crystallite Size (nm)	Crystallinity (%)
Anatase 100%	14.053	72.18
A_0 = X (90.6% R; 9.4% A)	10.382	63.69
A_1 = Y (83.0% R; 17.0% A)	11.252	57.16
A_2 = Z (50.2% R; 49.8% A)	12.611	52.16

Table 2. Textural Properties of Anatase TiO_2 and A_0, A_1, and A_2 Mixed-Phase TiO_2 Determined by N_2 Adsorption-Desorption Analysis

Sample	S_{BET} (m^2/g)	J (cm^3/g)	Pore Diameter (nm)
TiO_2 (anatase)	145.54	0.449	3.18
A_0	128.50	0.180	3.69
A_1	115.12	0.092	3.21
A_2	80.42	0.090	3.45

The anatase phase would transform into rutile at temperatures above 600°C (Ishigaki et al., 2020). In this study, the calcination was carried out at 400°C-a temperature generally insufficient to induce the anatase-to-rutile phase transition-for 2 h. However, this transformation may have been promoted during the sonication of the amorphous TiO_2 suspension in the presence of H_2O_2, as evidenced by the emergence of rutile diffraction peaks in the XRD pattern.

3.2 The Chemical Functionality and Surface Morphology

The FTIR analysis was conducted to identify surface functional groups and to support the structural characterization of the synthesized TiO_2. As shown in Figure 1, fully anatase TiO_2 exhibited characteristic absorption bands at 533, 1630, and 3213 cm^{-1}, corresponding to Ti–O–Ti stretching, H–O–H bending of adsorbed water, and O–H stretching of surface hydroxyl groups, respectively (Wahyuni et al., 2026). For the A_0 mixed phase with the addition of HNO_3 solution, the absorption bands were observed at 513, 1353, 1629, and 3213 cm^{-1}, which were assigned to Ti–O–Ti, N–O, H–O–H, and O–H vibrations, respectively. The appearance of a distinct band at 1353 cm^{-1} was attributed to N–O stretching, confirming the presence of nitrate (NO_3^-) residues introduced during the HNO_3 treatment (Al-Amin et al., 2025; Gibas et al., 2025). In comparison, the absorption bands at 525, 723, 1353, 1629, and 3234 cm^{-1} were observed for the A_1 mixed-phase TiO_2, while absorption bands at 533, 805, 1353, 1629, and 3006 cm^{-1} were observed for the A_2 mixed-phase TiO_2. The incorporation of H_2O_2 30% (10 mL for A_1 and 20 mL for A_2) induced the notable spectral changes. New bands at 723 cm^{-1} (in A_1) and 805 cm^{-1} (in A_2) were assigned to the oxygen-related species, likely associated with the formation of peroxo groups (–OOH) or modified Ti–O bonding resulted from the oxidative treatment (Gibas et al., 2024).

Additionally, the intensity of the bands at 1353 and 1629 cm^{-1} decreased upon the addition of H_2O_2, corresponding to N–O and H–O–H vibrations, respectively. This reduction indicated a lower nitrate residue and adsorbed water content, suggesting surface restructuring and purification during the modification process. The influence of H_2O_2 was further reflected in the O–H stretching region, where a shift to a higher wavenumber was observed (3234 cm^{-1}) for A_1 and to a lower wavenumber (3006 cm^{-1}) for A_2. These shifts implied the changes in the hydrogen-bonding environment and were likely associated with the surface chemical modification and possible alterations in the anatase–rutile phase composition of TiO_2 (Wu et al., 2016; Xie et al., 2024).

The SEM images in Figure 3 show the morphology of the fully anatase and the mixed-phase TiO_2. Based on the SEM images, the fully anatase TiO_2 exhibited a granular morphology, forming irregular agglomerates at the micrometer scale, with smaller primary grains interconnected to form compact secondary aggregates. The SEM images in Figure 3 demonstrate that the morphology of TiO_2 was strongly influenced by the anatase–rutile phase composition. The fully anatase

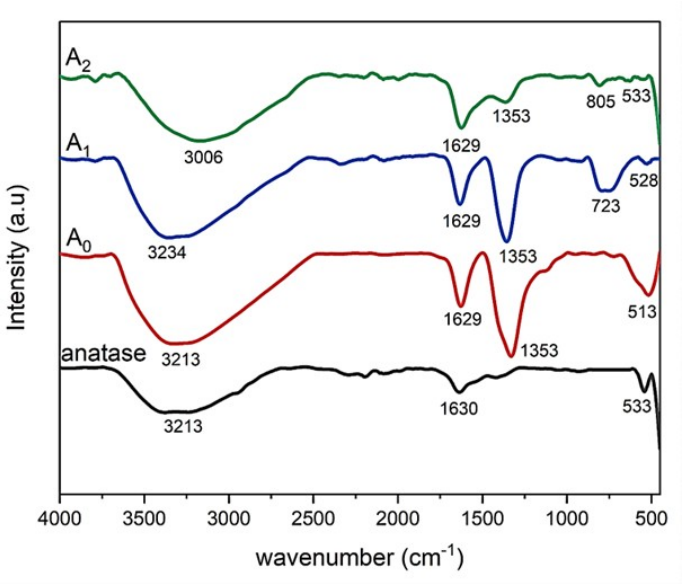

Figure 2. The FT-IR Spectra of the Fully Anatase and Mixed-Phase (A_0, A_1, and A_2) TiO_2

TiO_2 (100% anatase) exhibited a relatively open structure with uniformly distributed fine particles. This morphology reflected the dominance of the anatase phase, which typically formed smaller and less agglomerated particles. In A_0 TiO_2 (with 90.6% rutile), the surface morphology became more compact and tended to agglomerate with larger particle domains that was characteristic for rutile phase. The minor presence of anatase in A_0 mixed phase appeared as fine particles dispersed within larger aggregates, with limited impact on the overall structure. The A_1 mixed-phase TiO_2 (with 83.0% rutile) showed a more heterogeneous morphology, where anatase particles were increasingly distributed around rutile domains. This resulted in a less uniform structure, indicating stronger interfacial interactions between the two phases than in A_0. Meanwhile, the A_2 mixed-phase TiO_2 (≈50% rutile–anatase) exhibited the most heterogeneous and relatively porous morphology.

The anatase phase appeared to have a smoother surface texture, with smaller, more uniformly distributed grains, suggesting a higher specific surface area and a controlled crystal development without an excessive grain growth (Tovani et al., 2020). In contrast, the rutile phase displayed larger grains with a rougher, more consolidated texture, indicating a significant grain growth associated with its higher thermodynamic stability during thermal treatment (Bayati et al., 2013; Huang and Liu, 2014). The pronounced agglomeration observed in both phases implied strong interparticle interactions, likely mediated by Ti–O–Ti bridging bonds, resulting in dense, massive aggregate structures (Chelbi et al., 2020; Teamsinsungvon et al., 2022). Increasing the anatase fraction leaded to a more open, porous structure, whereas rutile-rich samples tended to form denser, more agglomerated morphologies. The formation of anatase-rutile heterojunctions in A_1 and A_{22} mixed

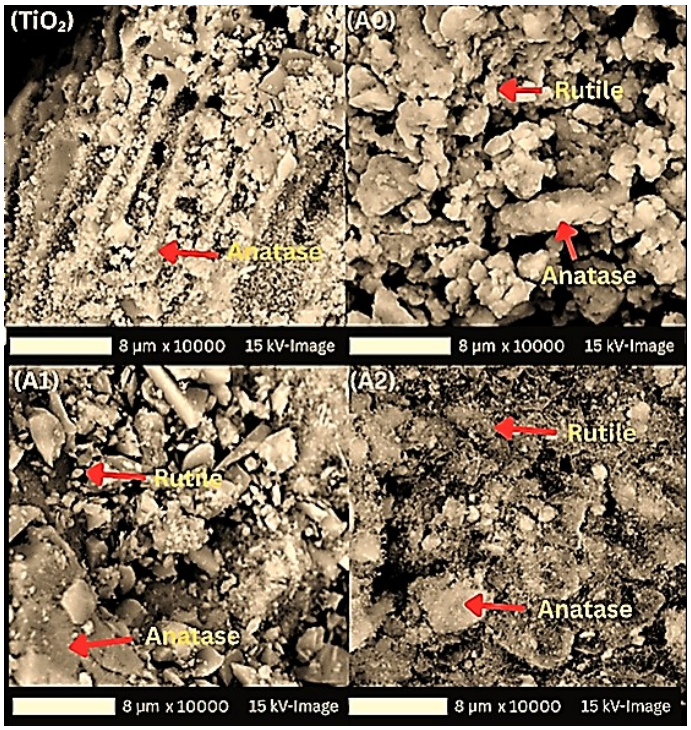

Figure 3. SEM Images of the Fully Anatase TiO_2 and the A_0, A_1, and A_2 mixed-phase TiO_2

phases was particularly important, as it provided interfacial sites that enhanced a charge separation, consistent with the reduced photo-luminescence intensity as observed.

The TEM images of A_2 mixed-phase TiO_2 (Figure 4) revealed that the synthesized TiO_2 particles exhibited an irregular morphology with a particle size ranging from 10-50 nm, which was consistent with the crystallite sizes calculated from XRD analysis using the Debye-Scherrer equation (10.382-14.053 nm). The TEM images indicated that particles tended to agglomerate due to strong interparticle interactions and high surface energy. The mixed-phase TiO_2 (A_0, A_1, and A_2) exhibited a more pronounced agglomeration than the fully anatase TiO_2, which correlated with the lower specific surface area observed through the BET analysis. This agglomeration behavior was consistent with the SEM observations and explained the reduction in specific surface area with increasing rutile fraction.

An EDS analysis for the A_2 mixed-phase TiO_2 (Figure 5) confirmed the presence of only titanium and oxygen in the synthesized A_2 samples, indicating its high phase purity and no detectable contaminants. The elemental composition analysis revealed an O/Ti atomic ratio in A_2 mixed phase TiO_2 of approximately 1.6, slightly lower than its stoichiometric value of 2.0, suggesting the possible existence of oxygen vacancies that may serve as active sites for photocatalytic reactions.

3.3 Optical Properties

The results of band gap analysis through DR-UV spectrophotometry processed using Tauc-plot (Kubelka-Munk) produced a curve as presented in Figure 6. Curve (a) shows the fully anatase TiO_2 band gap with a value of about 3.17 eV related to light absorption at wavelengths of 389-400 nm. On the curves A_0, A_1, and A_2, band gaps of 2.86, 2.80, and 2.75 eV were obtained, respectively, indicating that light absorption can occur at $\lambda > 400$ nm. These results showed a shift in light absorption towards the visible light.

The optical band gaps decreased from 3.17 eV for the fully anatase TiO_2 to 2.86, 2.80, and 2.75 eV for the A_0, A_1, and A_2 mixed-phase TiO_2, respectively, indicating the enhanced visible-light absorption. The anatase TiO_2 adopted a tetragonal structure with a better regularity, whereas the rutile TiO_2 gained a tetragonal structure with a more closed-packed system (Asahi et al., 2001). The combination of the anatase and rutile phases altered the energy band structure. At the anatase–rutile phase interface, a local electric field or heterojunction formed, which could effectively modify the band gap. The calcination process affected both the crystallinity and the band gap. In general, the mixed-phase anatase-rutile TiO_2 exhibited some changes in the crystal structure, including the formation of interphase interfaces, increased thermal stability, and changes in the crystal size. These changes affected the optical properties, i.e., the decrease in the band gap, thereby increasing the photo-response of materials in the visible-light region (Ishigaki et al., 2020; Lei et al., 2021; Zhang et al., 2010).

To further elucidate the optical properties, the absorption edges of the fully anatase and mixed-phase TiO_2 were explicitly determined from the UV-DRS spectra (inset of Figure 6). The absorption onset exhibited a systematic red shift from 392 nm for fully anatase TiO_2 to 430 nm (in A_0), 440 nm (in A_1), and 454 nm (in A_2). This progressive shift toward longer wavelengths corresponded to a narrowing of the optical band gap from 3.17 eV (anatase TiO_2) to 2.86, 2.80, and 2.75 eV (for A_0, A_1, and A_2, respectively). The observed band gap reduction could be attributed to the synergistic effect of anatase–rutile phase coupling and the formation of interfacial heterojunctions, which modified the electronic band structure and facilitate the charge transfer across the phase boundaries. Additionally, the post-hydrothermal treatment using HNO_3 and H_2O_2 likely introduced the oxygen vacancies and localized Ti^{3+} defect states below the conduction band, further narrowing the effective band gap. The extended absorption edge into the visible region ($\lambda > 400$ nm) enabled the mixed-phase TiO_2 (A_0, A_1, and A_2) to harvest a broader portion of the solar spectrum, thereby supporting their photocatalytic activity under a visible-light-containing irradiation. These optical modifications were consistent with the phase composition and structural evolution discussed in Sections 3.1 and 3.2.

The photoluminescence (PL) spectra in Figure 7 exhibited a broad visible emission band, with a dominant peak at ~476–479 nm for all samples. Such broad emission characteristics indicated the predominance of defect-mediated transitions, particularly those associated with oxygen vacancies and surface trap states, which were commonly recombination centers in TiO_2-based materials (Pallotti et al., 2017; Rajabi et al.,

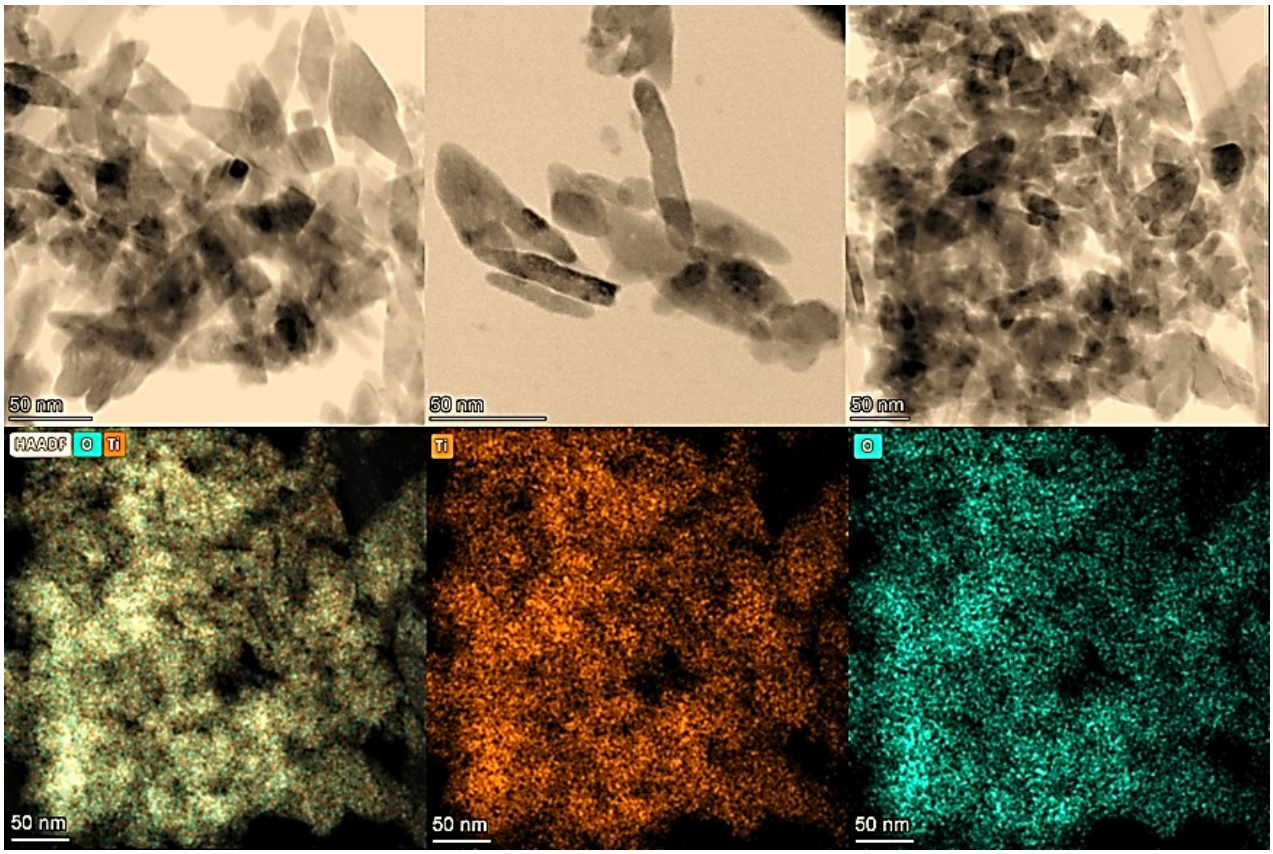

Figure 4. TEM Image of the A_2 mixed phase TiO_2

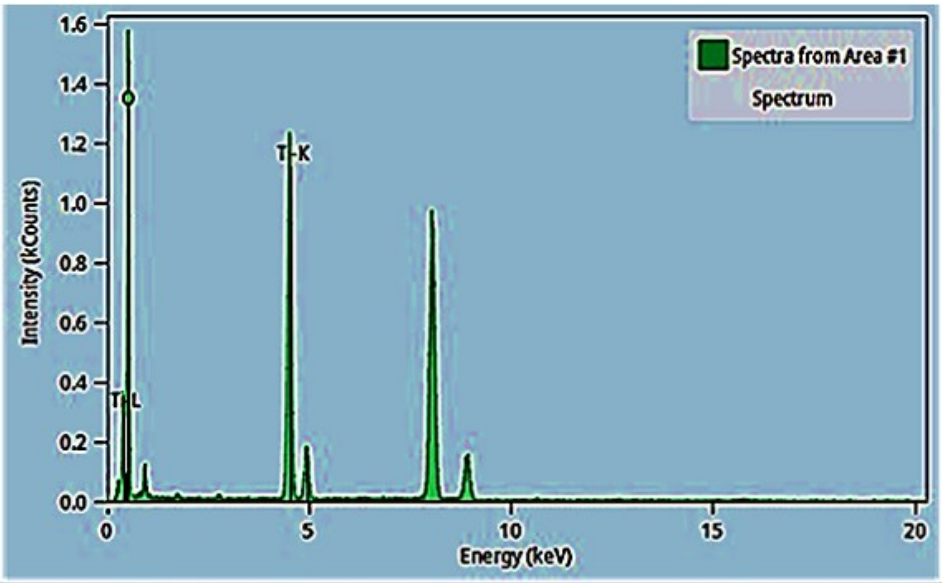

Z	Element	Family	Atomic Fraction (%)	Atomic Error (%)	Mass Fraction (%)	Mass Error (%)	Fit Error (%)
8	O	K	63.46	3.92	36.72	3.93	0.56
22	Ti	K	36.54	3.92	63.28	3.93	0.08

Figure 5. EDS Spectra of the Synthesized A_2 Mixed phase TiO_2

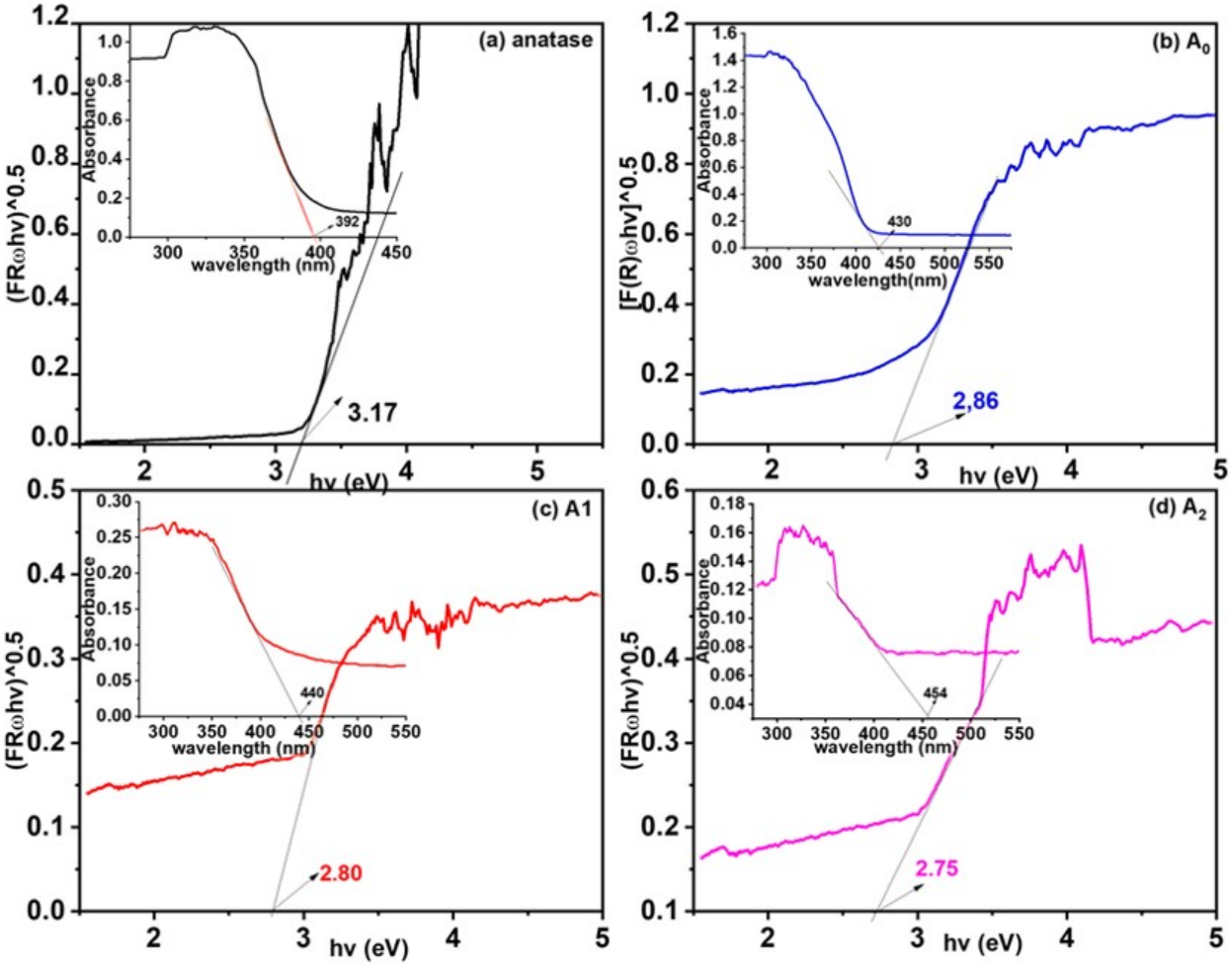

Figure 6. Tauc Plots $[F(R)h\nu]^{0.5}$ vs. $h\nu$ for Band Gap Determination of (a) Anatase, (b) A_0, (c) A_1, and (d) A_2 Samples. The Insets Show the Corresponding UV-DRS Absorption Spectra with Absorption Edges at 392, 430, 440, and 454 nm, Respectively

2015). The fully anatase TiO_2 exhibited a maximum emission at 478.8 nm, while the A_0 mixed-phase TiO_2 showed a slight blue shift to 476.9 nm. Moreover, the A_1 and A_2 mixed-phase TiO_2 maintained nearly identical peak positions at 477 nm. This shift toward shorter wavelengths suggested a reduction in shallow defect states or improved local structural ordering (Chen et al., 2019; Murawski et al., 2023).

More importantly, the most pronounced change was observed in the PL emission intensity. The fully anatase TiO_2 exhibited the highest emission intensity, indicating a high rate of radiative electron–hole recombination (Bulyarskiy et al., 2020; Rajabi et al., 2015). In contrast, the progressive decrease in the PL intensity upon H_2O_2 addition reflected a suppression of recombination centres, implying a significant reduction in the defect density. This observation highlighted the role of H_2O_2 not only as an oxidizing agent but also as an effective surface chemical modifier that reduced oxygen vacancy concentrations.

From a mechanistic perspective, the decrease in photoluminescence (PL) intensity could be attributed to a reduced population of trap states associated with oxygen vacancies acting as both radiative and non-radiative recombination centres. Therefore, the attenuation of PL intensity in this region indicated a reduction in these defect-related states. Importantly, these findings implied an increase in the charge-separation efficiency, as the reduction in recombination centres allowed for longer carrier lifetimes (Zhang et al., 2025). Although the variation in band gap energy was relatively small, the modification of defect states played a more critical role in determining the material's optoelectronic performance.

3.4 Surface Area and Textural Properties

Surface area analysis using the BET method resulted in an adsorption-desorption curve as shown in Figure 8. The difference in the shape of the curve indicated a change in the surface characteristics of the anatase TiO_2 and the mixed-phase TiO_2. There is a relationship between the type of "hysteresis loop" and surface texture, i.e., pore size distribution, pore geometry,

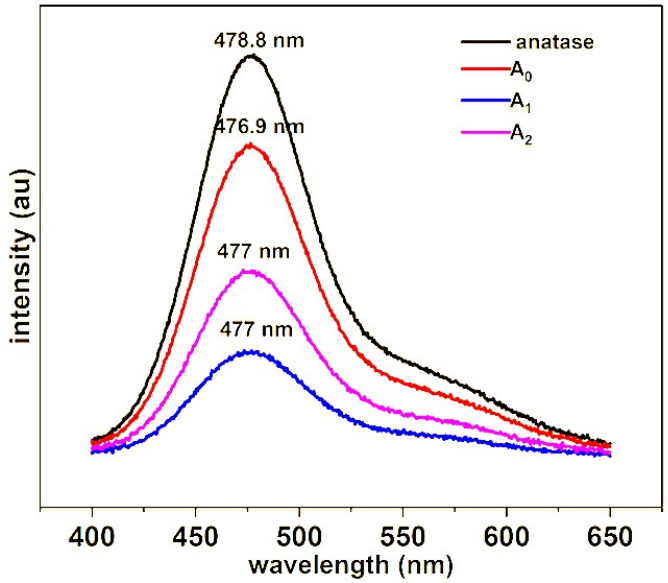

Figure 7. Photoluminescence (PL) Spectra of the Fully Anatase TiO_2 and the A_0, A_1, dan A_2 Mixed-Phase TiO_2

and pore connectivity. The isothermal curve of anatase TiO_2 included type IV with a "hysteresis loop" of H1 type at a relative pressure of 0.8 according to the IUPAC classification. This related to pores resembling evenly distributed, cylindrical canals (Carja et al., 2001). The isotherm curve of A0 mixed phase belonged to an isotherm of type IV with a "hysteresis loop" of H4 type, associated with narrow-slit pores in the micropore region. The isothermal curves for A_1 and A_2 mixed phases showed a "hysteresis loop" of H3 type, indicating no adsorption restriction at high P/Po, with a layered surface of plate-like particles that formed slit-shaped pores. The desorption model for H3-type hysteresis also included steep regions associated with forced closure of the hysteresis loop, resulting from tensile forces (Donohue and Aranovich, 1998).

A surface texture analysis was performed using a BJH desorption and is presented in Table 2. The S_{BET} values decreased progressively from anatase TiO_2 (145.54 m^2/g) to A_0 (128.50 m^2/g), A_1 (115.12 m^2/g), and A_2 (80.42 m^2/g). A similar trend was observed for the total pore volume, which declined from 0.449 cm^3/g (for anatase TiO_2) to 0.090 cm^3/g (A_2).

The average pore diameters remained within a narrow mesoporous range (3.18-3.69 nm) across all samples, indicating a relatively uniform pore structure despite variations in the phase composition. The pore shape became smaller and narrower due to a partial phase shift of TiO_2 from anatase to rutile with a closer lattice spacing. This change in pore shape can also be predicted from the shape of the hysteresis loop on its isothermal curve (Fan et al., 2013). The changes in the pore morphology of TiO_2 after shifting the crystallite phase composition were also reported in the studies conducted by Vaez et al. (2018). The reduction in the surface area and pore volume in the mixed-phase TiO_2 might be attributed to the particle agglomeration and/or densification of the crystal structure, as supported by SEM observations and XRD analysis showing changes in crystallinity. These BJH-derived textural parameters, combined with XRD crystallite size data and TEM observations, provided a comprehensive understanding of the structural characteristics that influenced the photocatalytic performance. Therefore, the current suite of characterization techniques has sufficiently described the particle morphology and porosity for this solid-state photocatalytic system.

3.5 The Photocatalytic Activity of Mixed-Phase TiO_2 for Rhodamine-B Degradation

The effects of phase composition and specific surface area on the photocatalytic performance of all TiO_2 samples were studied by monitoring the degradation of Rh-B under irradiation using LED-UV lamps. Figure 9 shows the adsorption performance and photocatalytic activity of both anatase TiO_2 and mixed-phase TiO_2 (A_0, A_1, and A_2). Before irradiation, the adsorption-desorption equilibrium was established in the dark for 30 min. Figure 9 explicitly presents the adsorption performance of each catalyst. The results showed that the anatase TiO_2 exhibited the highest adsorption capacity, removing 56.7% of Rh-B. The mixed-phase TiO_2 (A_0, A_1, and A_2) showed a comparable adsorption performance, removing 56.4%, 56.2%, and 56.2% of the initial Rh-B, respectively. This consistent initial adsorption confirmed that the subsequent decrease in the Rh-B concentration under irradiation (reaching 96.7–98.2% for anatase TiO_2 and 91–93.8% for mixed-phase TiO_2) was due to the photocatalysis. A blank test was also conducted, showing negligible adsorption (14.7%) and photolysis (20.4%) without the presence of a catalyst, further confirming the necessity of the photocatalyst for effective degradation.

Contrary to the general expectation that the mixed-phase TiO_2 would exhibit a superior photocatalytic performance compared to the fully anatase TiO_2, this study demonstrated that fully anatase TiO_2 achieved higher degradation efficiency (96.7-98%) compared to the A_0, A_1, and A_2 mixed-phase TiO_2 (90.5-93.8%). This finding warranted a critical discussion to reconcile the apparent contradiction with literature reports.

Previous studies have consistently reported that mixed-phase TiO_2 with an optimal composition of 70-80% anatase and 20-30% rutile exhibited an enhanced photocatalytic activity due to the synergistic effects, including improved charge separation at the anatase-rutile interface and extended light absorption range (Bagheri and Julkapli, 2017; Cheng et al., 2014). However, the photocatalytic performance of the mixed-phase TiO_2 was highly dependent on achieving this optimal phase ratio, which was not attained in the present study. The inferior performance of the mixed-phase TiO_2 reported in this study could be attributed to several interconnected factors, as follows.

1. **Non-optimal Phase Composition.** The synthesized mixed- phase TiO_2 contained anatase fractions of 9.4% (A_0), 17% (A_1), and 49.8% (A_2), all of which fell below the reported optimal range. When the rutile phase domi-

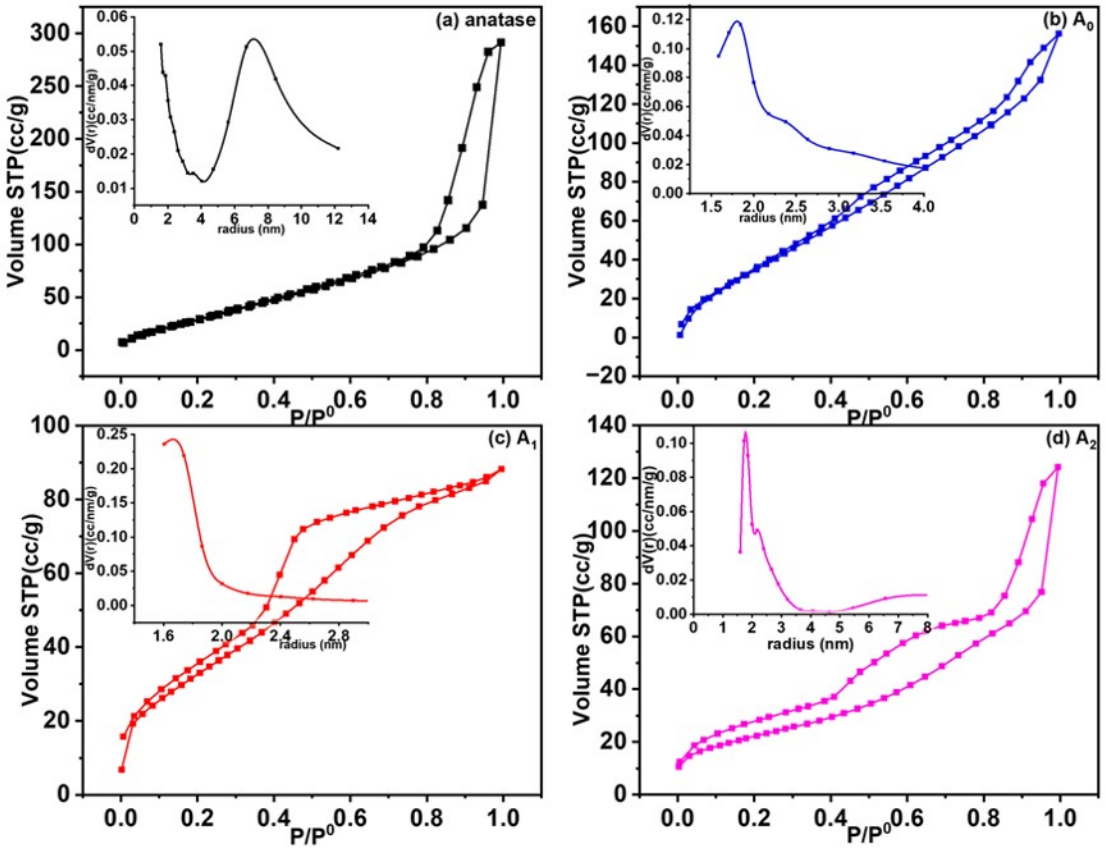

Figure 8. Adsorption-Desorption Curve of Anatase TiO_2 and A_0, A_1, and A_2 mixed phase TiO_2

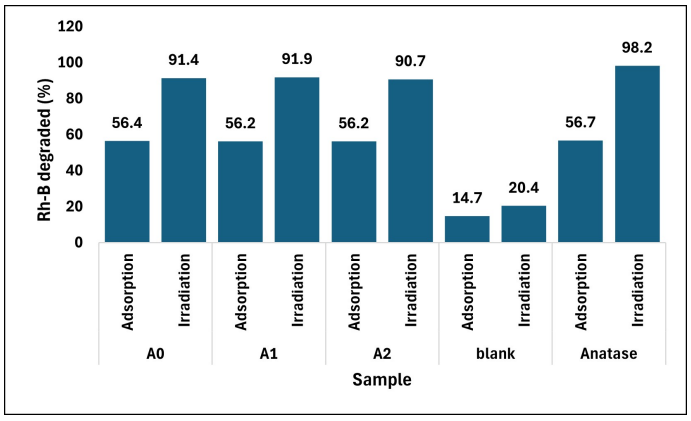

Figure 9. The photocatalytic Performance of Anatase TiO_2 and A_0, A_1, A_2 mixed phase TiO_2 during the degradation of Rh-B

nated excessively (as in A_0 and A_1), the beneficial heterojunction effect was diminished as there were insufficient anatase domains to serve as the primary photocatalytically active component. In the case of the A_2 mixed-phase TiO_2, despite having a nearly equal anatase-rutile ratio, it still did not achieve the optimal composition that maximized the synergistic effects.

2. **Specific Surface Area**. The specific surface area decreased significantly with increasing rutile content: anatase (143.535 m^2/g) > A_0 (128.503 m^2/g) > A_1 (115.119 m^2/g) > A_2 (80.415 m^2/g). The larger surface area of the fully anatase TiO_2 provided more active sites for Rh-B adsorption and subsequent photocatalytic degradation. This was corroborated by the adsorption data, which showed that the anatase TiO_2 adsorbed 54.6% of Rh-B during the dark equilibrium period, compared to only 36.9-49.3% for the mixed-phase TiO_2.
3. **Crystallinity and Crystallite Size**. The fully anatase TiO_2 exhibited the highest crystallinity (72.18%) and largest crystallite size (14.053 nm) among all samples. Higher crystallinity would reduce the density of the defect sites that served as the recombination centers for the photogenerated electron-hole pairs. The larger crystallite size in the fully anatase TiO_2 also facilitated a longer migration distance for the charge carriers before reaching the surface, promoting more efficient charge separation and transfer (Wang et al., 2020; Zhang et al., 2014).
4. **Phase Transformation Effects**. The formation of the rutile phase during the synthesis (despite calcination at only 400 °C) was likely induced by the ultrasonic irradiation in HNO_3 solution. This unconventional phase formation

pathway may have led to different interfacial characteristics compared to the thermally induced phase transformation, potentially affecting the quality of anatase-rutile heterojunctions and the charge-transfer efficiency.

5. **Band Gap vs. Surface Properties Trade-off**. Although the mixed-phase TiO_2 exhibited narrower band gaps (2.75-2.86 eV) compared to anatase (3.17 eV), enabling visible light absorption, this advantage was outweighed by the superior surface properties (surface area, adsorption capacity, crystallinity) of pure anatase under the UV-LED irradiation conditions employed in this study. This finding emphasized that band gap engineering alone was insufficient to enhance the photocatalytic performance if it compromised other critical material properties. These results highlighted that preparing a high-performance mixed-phase TiO_2 required a precise control over the anatase-rutile ratio, which was not fully achieved in the current synthesis protocol. Future work should focus on optimizing the HNO_3/H_2O_2 mole ratio and synthesis conditions to achieve the target composition of 70–80% anatase and 20–30% rutile, which was expected to maximize the synergistic effects between the two phases (Wang et al., 2020; Zhang et al., 2014).

For the photocatalytic tests using the mixed-phase TiO_2 (A_0, A_1, and A_2), three repetitions were performed to assess their possible reusability. Figure 10 shows the performance of the mixed-phase TiO_2 to reduce the Rh-B concentration after the first, second and third use. The second and third activity tests still showed a reduction in Rh-B concentration up to 80%. The relatively high performance of the anatase-rutile mixed-phase TiO_2 could be due to its lower band gap energy, according to the absorbance-reflectance analysis, ranging from 2.75–2.86 eV. These band gaps were equivalent to the energy at $\lambda > 410$ nm (in the initial region of visible light). Therefore, the photocatalytic process driven by LED and UV rays could proceed even though the rutile phase was predominant.

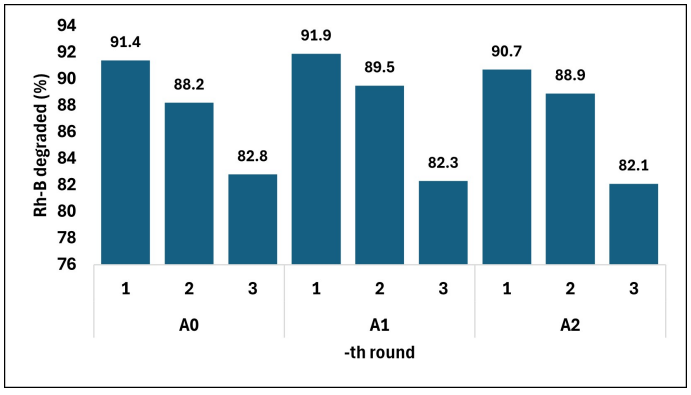

Figure 10. The Photocatalytic Performance of the A_0, A_1, dan A_2 Mixed-Phase TiO_2 in a Three-Round Test

In general, the photocatalytic process would involve steps of excitation, diffusion, transfer of photon-induced charge carriers to the surface, and radical chain reactions. Only a separate charge carrier would participate in the following radical chain reaction. For a single phase of TiO_2, most photon-hole pairs (e^-h^+) would usually quickly recombine again in the phase or at the surface site, accompanied by a photon discharge and heat, resulting in a photoluminescent (PL) spectrum. Therefore, the PL spectra could be used to compare the recombination rate of the pairs (e^-h^+) produced by photons in several different photocatalysts (Cheng et al., 2014).

The photocatalytic mechanism could be illustrated using a simple yet clear diagram. Figure 11 explicitly illustrates the proposed photocatalytic mechanism. The figure depicts the band alignment of anatase (~3.2 eV) and rutile (~3.0 eV), the formation of anatase-rutile heterojunctions, and the directional transfer of photogenerated charge carriers: electrons migrate from the rutile conduction band to the anatase conduction band, while holes transfer from the anatase valence band to the rutile valence band. This spatial separation would effectively suppress the electron-hole recombination and facilitate the generation of reactive oxygen species (•OH on the anatase valence band and $\bullet O_2^-$ on the rutile conduction band), which subsequently drive the oxidative degradation of organic pollutants into CO_2 and H_2O.

The activity tests on all TiO_2 samples were also performed to determine the degradation rate of Rh-B as a function of irradiation time with a 120-min adsorption step overall. A graph of the degradation rate is shown in Figure 12. The fully anatase TiO_2 showed the highest degradation rate, while A_2 showed the lowest. The high degradation rate when the fully anatase TiO_2 was used, probably was due to its largest band gap (3.07 eV) and specific surface area (143.535 m^2/g). In the case of the A_2 mixed-phase TiO_2, although A_2 and A_1 had almost the same band gap value, the specific surface area of A_1 was greater than that of A_2. In summary, the difference in specific surface area had a greater effect on the rate of Rh-B degradation during this activity test.

In a similar study observing the photocatalytic activity of TiO_2, it was reported that TiO_2 treated with a high-temperature calcination (700-900 °C) showed a photocatalytic activity in the visible light region while the degradation efficiency was not specified (Ishigaki et al., 2020). In this study, the anatase and mixed-phase anatase-rutile TiO_2 were only treated with calcination up to 400 °C. However, the efficiency of TiO_2 as a mixed-phase photocatalyst in this study was relatively high (> 91%), whereas most semiconductor-based photocatalysts exhibited a relatively low efficiency due to their low photonic efficiency (< 10%) (Irie et al., 2003b). Therefore, much effort has been devoted to the design of photocatalytic systems that leaded to high light conversion efficiency (Wang et al., 2009). In this study, it was observed that the fully anatase TiO_2 showed a greater adsorption capacity for organic compounds than rutile, although it exhibited a lower recombination rate due to its higher band gap. Therefore, it also could show the most active photochemical properties (Aman et al., 2016; Yu et al., 2002).

The differences in properties between the anatase and ru-

Table 3. A Comparison of the Photocatalytic Performance of vVarious Anatase-Rutile TiO_2 Systems During the Rh-B Degradation

Sample	A/R Ratio	Synthesis Method	Light Source	Catalyst Dose (g/L)	Initial [Rh-B] (ppm)	Degradation (%)	Time (min)	Reference
Pure Anatase	100:0	Sol-gel + hydrothermal	LED 100W + UV (40W)	1	25	98	90	This work
A_0	9.4:90.6	Sol-gel + hydrothermal	idem	1	25	85	90	This work
A_1	17:83	Sol-gel + hydrothermal	idem	1	25	88	90	This work
A_2	49.8:50.2	Sol-gel + hydrothermal	idem	1	25	91	90	This work
Pure Anatase	100:0	Low-temperature synthesis	UV (300W Xe)	1	10	~95	120	(Zhang et al., 2011)
Pure Rutile	0:100	Low-temperature synthesis	idem	1	10	~85	120	(Zhang et al., 2011)
P25 (Degussa)	~80:20	Commercial	idem	1	10	~92	120	(Zhang et al., 2011)
Mixed phase	77:23	Hydrothermal (tartaric acid)	UV	1	20	~94	180	(Li et al., 2015)
Biphasic TiO_2	90.3:9.7	Hydrothermal (H_2O_2/HNO_3)	Xe lamp (300W)	1	20 (MB)°	100	30	(Wang et al., 2020)
Anatase/Rutile	70:30	Sol-gel	UV	0.5	10	~96	150	(Bojinova et al., 2007)
Mixed phase	50:50	Non-aqueous sol-gel	Visible	1	10	~88	180	(Liu et al., 2016)
Mixed phase	69:31	Polyol-solid surface/interface transesterification	Xenon lamp 300 Watt	0.4	20	98.71	90	(Zhang et al., 2025)

MB° = Methylene Blue (for Wang et al. study)

tile phases were a consideration, as the combination of the two phases could suppress the recombination rate and increase the light absorption efficiency (Irie et al., 2003a; Kacem et al., 2017). If the combination of the anatase-rutile phases resulted in a relative alignment of the conduction bands at their edges, the efficiency of light absorption would increase (Cheng et al., 2015). However, differences in the structures of rutile and anatase resulted in distinct paramagnetic properties of the trapped electrons, which affected the electron transfer pathway and the photocatalytic activity of mixed-phase TiO_2 (He et al., 2016; Zhou et al., 2015).

The crystallinity of the fully anatase TiO_2 was higher than that of the anatase-rutile mixed-phase. Therefore, its higher photocatalytic activity of the former compared to that of the latter was observed in this study. The anatase phase would serve as the active component of the photocatalyst, while the rutile phase would act as an electron absorber (Chen et al., 2016; Zhao et al., 2015). It was also found that photocatalytic activity and selectivity were highly dependent on the phase composition ratios (Wang et al., 2009; Zhang et al., 2015). The composition of these phases would affect the adsorption ability of the reactant molecules and the efficient transfer of electrons from the surface site to the TiO_2 conduction band in the mixed phase. Thus, the synergy between adsorption, radiation, and photon-induced charge-carrier separation, as well as the occurrence of redox reactions over a large specific surface area, was responsible for the overall improvement in photocatalytic properties (Baccaro et al., 2023; Daimon and

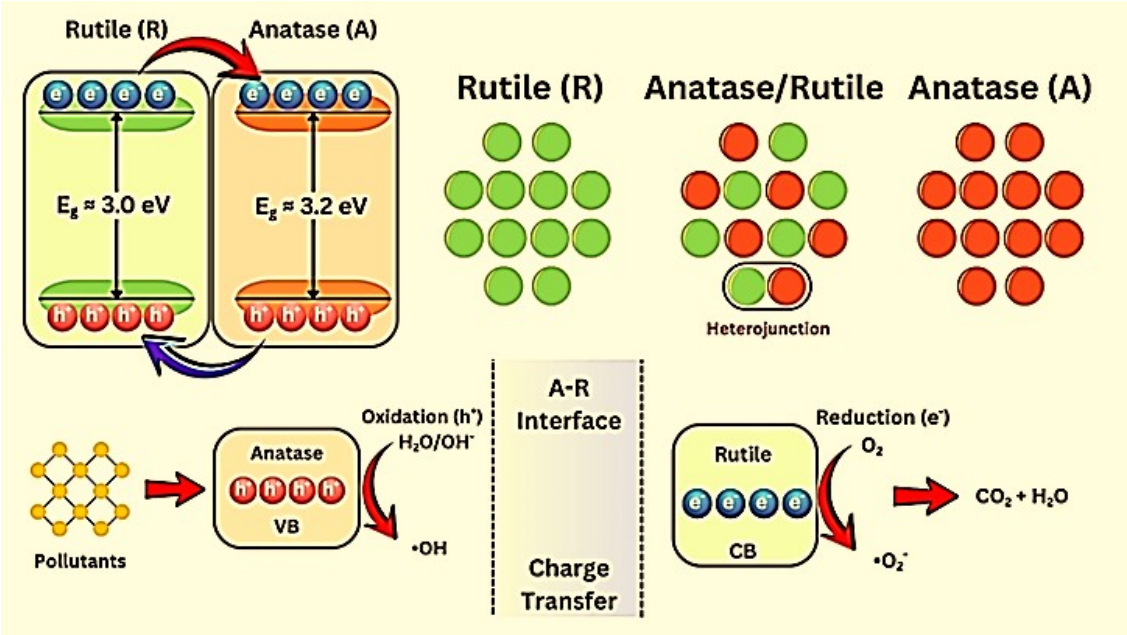

Figure 11. The Photocatalytic Mechanism of Pollutant Degradation Using the Mixed-Phase TiO_2 as a Catalyst

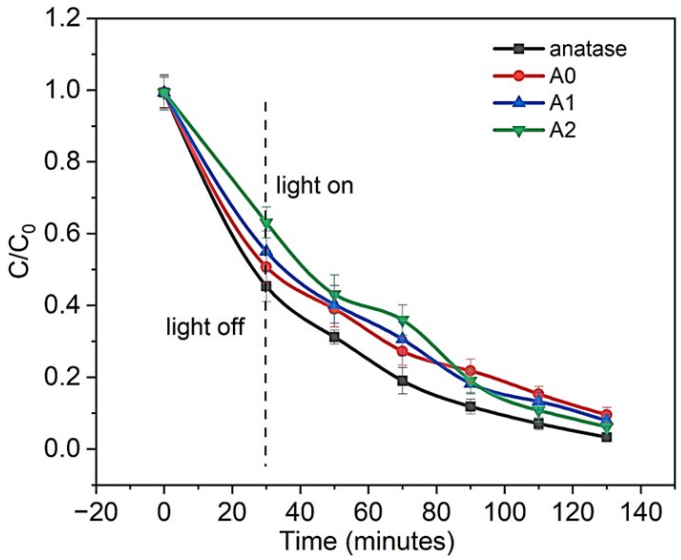

Figure 12. The Rate of Rh-B Degradation by the Fully Anatase and Mixed-Phase (A_0, A_1, dan A_2) TiO_2

Nosaka, 2007). In most cases, the combination of anatase and rutile structures with the composition of (70-80%) anatase and (20-30%) rutile in the mixed-phase TiO_2 resulted in a better photocatalytic performance compared to the fully anatase TiO_2 (Bagheri and Julkapli, 2017; Cheng et al., 2014).

As summarized in Table 3, the photocatalytic performance of the synthesized anatase TiO_2 in this study compared favorably with previously reported systems, achieving 96.7-98% Rh-B degradation within 90 min. Despite of its lower activity compared to the fully anatase TiO_2, the mixed-phase TiO_2 demonstrated a moderate activity (85–91%), due to their enhanced visible-light response because of their narrower band gaps. This suggested that the mixed-phase TiO_2 showed a potential for solar-driven applications with further optimization of the anatase-rutile ratio.

To quantitatively evaluate the photocatalytic performance of the mixed-phase TiO_2 and understand the reaction mechanism of TiO_2-catalyzed Rh-B degradation, the experimental data were analysed using a pseudo-first-order kinetic model based on the Langmuir-Hinshelwood equation, expressed in Equation (4), where C_0 is the initial concentration of Rh-B, C is the concentration of Rh-B at irradiation time t, and k is the apparent rate constant (min^{-1}).

$$-\ln\left(\frac{C}{C_0}\right) = kt \tag{4}$$

Figure 13 shows the linear plots of $-\ln(C/C_0)$ versus irradiation time for all TiO_2 samples. The high correlation coefficients ($R^2 > 0.97$) obtained for all samples confirming that the photocatalytic degradation of Rh-B followed a pseudo-first-order kinetics under the experimental conditions used in this study.

The apparent rate constants (k) were determined from the slopes of the linear plots as summarized in Table 4. The fully anatase TiO_2 exhibited the highest rate constant of 0.02656 min^{-1} with R^2 of 0.98955, which was approximately 1.5 times higher than that of the mixed-phase A_0 TiO_2 (k of 0.01791 min^{-1}). The rate constants decreased in the following order: fully anatase TiO_2 (0.02656 min^{-1}) > A_2 (0.02264 min^{-1}) > A_1 (0.02011 min^{-1}) > A_0 (0.01791 min^{-1}).

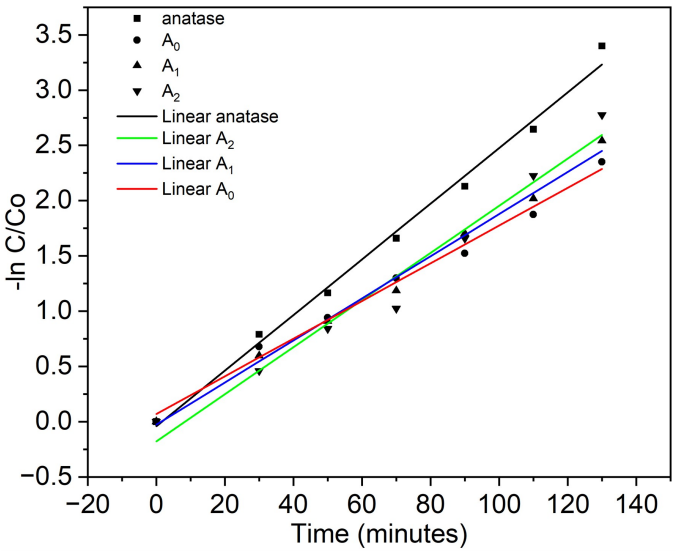

Figure 13. The Linear Plots of -ln(C/C$_0$) Versus Irradiation Time During the Degradation of Rh-B Using Anatase and Mixed-Phase TiO_2

Table 4. The Apparent Rate Constants (k) Calculated from the Slopes of the Linear Photocatalyst

Photocatalyst	k (menit^{-1})	R^2	% degradation Rh-B
TiO_2	0.0266	0.9896	96.7
A_0	0.0179	0.9765	90.5
A_1	0.0201	0.9901	92.1
A_2	0.0226	0.9783	93.8

This trend correlated well with the specific surface area and crystallinity of the photocatalysts. The fully anatase TiO_2, with the largest specific surface area (143.535 m^2/g) and highest crystallinity (72.18%), provided more active sites for adsorption and photocatalytic reaction, resulting in the highest degradation rate. The mixed-phase A_2 TiO_2, despite having a mixed-phase composition of 49.8% anatase and 50.2% rutile with a narrower band gap (2.75 eV), showed a lower rate constant compared to the fully anatase TiO_2 due to its smaller specific surface area (80.415 m^2/g) and lower crystallinity (52.16%).

Interestingly, among the mixed-phase TiO_2, A_2 exhibited the highest rate constant, followed by A_1 and A_0. This trend suggested that increasing the anatase content in the mixed-phase system enhanced the photocatalytic activity, though it still could not surpass that of the fully anatase TiO_2. The relatively high R^2 values (0.9765-0.9901) for all TiO_2 samples indicated an excellent linearity and confirmed the validity of the pseudo-first-order kinetic model in describing the photocatalytic degradation process.

The better performance of the fully anatase TiO_2 could be attributed to several factors: (1) higher specific surface area providing more active sites for Rh-B adsorption, (2) better crystallinity reducing defect-mediated recombination centers, and (3) optimal crystallite size (14.05 nm) facilitating an efficient charge carrier migration to the surface. Although the mixed-phase TiO_2 showed narrower band gaps (2.75-2.86 eV) enabling a visible-light absorption, the synergistic effect between the anatase and rutile phases was insufficient to overcome the advantages of pure anatase under UV-LED irradiation in this study.

The kinetic analysis results in this study were consistent with the degradation efficiency data, where the fully anatase TiO_2 achieved 96.7-98% degradation, while the mixed-phase TiO_2 showed degradation efficiencies ranging from 90.5% to 93.8%. These findings emphasized that, under the experimental conditions employed, the specific surface area and crystallinity play a more dominant role in determining the photocatalytic activity than the phase composition or band gap narrowing.

4. CONCLUSION

This study has produced several important findings, detailed as follows: The moles of HNO_3 and H_2O_2 as peptide agents affected the formation of anatase-rutile mixed-phase after hydrothermal treatment during the TiO_2 synthesis. In this study, the mole ratio HNO_3/H_2O_2 of 0.153 produced mixed-phase TiO_2 with a composition of 49.8% A (anatase) and 50.2% R (rutile). The photocatalytic degradation of Rh-B using the anatase-rutile mixed-phase TiO_2 resulted in 91–93.6% degradation, slightly lower than that of the fully anatase TiO_2 (96.7–98%). This study still requires the development and investigation of different mole ratios of HNO_3/H_2O_2 to obtain the optimal composition of anatase-rutile (80%–20%) and to examine the photocatalytic activity for a wider application. Future studies would systematically investigate the effects of operational parameters (i.e., catalyst loading, pollutant concentration, pH) and conduct detailed kinetic modeling to optimize the photocatalytic performance of H_2O_2-regulated mixed-phase TiO_2 for practical applications.

5. ACKNOWLEDGMENT

The authors would like to thank the Institute for Research and Community Service, Universitas Negeri Semarang, for the financial support through the Fundamental Research Scheme Program, with a contract No. 20.12.4/UN37/PPK.10/2023, dated 12 April 2023. The authors would also like to thank the Guinevere Shop for assisting with the data analysis.

REFERENCES

Ahmed, S., M. K. H. Shishir, M. T. Islam, M. A. Rahaman, S. Aman, A. R. Aidid, S. I. Sadia, M. M. Rana, and M. A. Alam (2025). Crystallinity Integration of Anatase (TiO_2) Nanocrystal by Whole Powder Pattern Fitting (WPPF) Method: A Rietveld Refinement Study. *Results in Materials*, **26**; 100673

Al-Amin, K., M. Kawsar, M. T. R. B. Mamun, and M. Sahadat Hossain (2025). Fourier Transform Infrared Spec-

troscopic Technique for Analysis of Inorganic Materials: A Review. *Nanoscale Advances*, **7**(21); 6677–6702

Aman, N., N. N. Das, and T. Mishra (2016). Effect of N-Doping on Visible Light Activity of TiO_2-SiO_2 Mixed Oxide Photocatalysts. *Journal of Environmental Chemical Engineering*, **4**(1); 191–196

Asahi, R., T. Morikawa, T. Ohwaki, K. Aoki, and Y. Taga (2001). Visible-Light Photocatalysis in Nitrogen-Doped Titanium Oxides. *Science*, **293**(5528); 269–271

Baccaro, A. L. B., C. C. Seki, F. G. Nishimura, L. D. Cordon, L. A. C. Carvalho, and I. G. R. Gutz (2023). Effectiveness of Metal–EDTA-Polluted Water Treatment and Metal Recovery at Drop-Casted Films of TiO_2 Under UV-LED Irradiation: A Photoelectrochemical Study. *Results in Chemistry*, *5*

Bagheri, S. and N. M. Julkapli (2017). Mixed-Phase TiO_2 Photocatalysis: Correlation Between Phase Composition and Photodecomposition of Water Pollutants. *Reviews in Inorganic Chemistry*, **37**(1); 11–28

Bayati, M. R., S. Joshi, R. J. Narayan, and J. Narayan (2013). Low-Temperature Processing and Control of Structure and Properties of TiO_2/c-Sapphire Epitaxial Heterostructures. *Journal of Materials Research*, **28**(13); 1669–1679

Bojinova, A., R. Kralchevska, I. Poulios, and C. Dushkin (2007). Anatase/Rutile TiO2 Composites: Influence of the Mixing Ratio on the Photocatalytic Degradation of Malachite Green and Orange II in Slurry. *Materials Chemistry and Physics*, **106**(2–3); 187–192

Bokov, D., A. Turki Jalil, S. Chupradit, W. Suksatan, M. Javed Ansari, I. H. Shewael, G. H. Valiev, and E. Kianfar (2021). Nanomaterial by Sol-Gel Method: Synthesis and Application. *Advances in Materials Science and Engineering*, **2021**(1)

Bulyarskiy, S. V., V. S. Gorelik, G. G. Gusarov, D. A. Koiva, and A. V. Lakalin (2020). The Influence of Electron–Phonon Interaction on Photoluminescence of Titanium Oxide in the Near-Infrared Spectral Range. *Optics and Spectroscopy*, **128**(5); 590–595

Chelbi, S., D. Djouadi, A. Chelouche, L. Hammiche, T. Touam, and A. Doghmane (2020). Effects of Ti-Precursor Concentration and Annealing Temperature on Structural and Morphological Properties of TiO_2 Nano-Aerogels Synthesized in Supercritical Ethanol. *SN Applied Sciences*, **2**(5); 872

Chen, C., F. Chen, X. Chen, B. Deng, B. Eng, D. Jung, Q. Guo, S. Yuan, K. Watanabe, T. Taniguchi, M. L. Lee, and F. Xia (2019). Bright Mid-Infrared Photoluminescence from Thin-Film Black Phosphorus. *Nano Letters*, **19**(3); 1488–1493

Chen, X., D.-H. Kuo, D. Lu, Y. Hou, and Y.-R. Kuo (2016). Synthesis and Photocatalytic Activity of Mesoporous TiO_2 Nanoparticle Using Biological Renewable Resource of Un-Modified Lignin as a Template. *Microporous and Mesoporous Materials*, **223**; 145–151

Cheng, H., J. Wang, Y. Zhao, and X. Han (2014). Effect of Phase Composition, Morphology, and Specific Surface Area on the Photocatalytic Activity of TiO_2 Nanomaterials. *RSC Advances*, **4**(87); 47031–47038

Cheng, X., Q. Cheng, B. Li, X. Deng, J. Li, P. Wang, B. Zhang, H. Liu, and X. Wang (2015). One-Step Construction of N/Ti^{3+} Codoped TiO_2 Nanotubes Photoelectrode with High Photoelectrochemical and Photoelectrocatalytic Performance. *Electrochimica Acta*, **186**; 442–448

Christy, P. D., N. Melikechi, N. S. Nirmala Jothi, A. R. Baby Suganthi, and P. Sagayaraj (2010). Synthesis of TiO_2 Nanorods by Oriented Attachment Using EDTA Modifier: A Novel Approach Towards 1D Nanostructure Development. *Journal of Nanoparticle Research*, **12**(8); 2875–2882

Daimon, T. and Y. Nosaka (2007). Formation and Behavior of Singlet Molecular Oxygen in TiO_2 Photocatalysis Studied by Detection of Near-Infrared Phosphorescence. *The Journal of Physical Chemistry C*, **111**(11); 4420–4424

Donohue, M. D. and G. L. Aranovich (1998). Adsorption Hysteresis in Porous Solids. *Journal of Colloid and Interface Science*, **205**(1); 121–130

Eddy, D. R., M. D. Permana, L. K. Sakti, G. A. N. Sheha, G. A. N. Solihudin, S. Hidayat, T. Takei, N. Kumada, and I. Rahayu (2023). Heterophase Polymorph of TiO_2 (Anatase, Rutile, Brookite, TiO_2(B)) for Efficient Photocatalyst: Fabrication and Activity. *Nanomaterials*, **13**(4); 704

El-Desoky, M. M., I. Morad, M. H. Wasfy, and A. F. Mansour (2020). Synthesis, Structural and Electrical Properties of PVA/TiO_2 Nanocomposite Films with Different TiO_2 Phases Prepared by Sol–Gel Technique. *Journal of Materials Science: Materials in Electronics*, **31**(20); 17574–17584

Fan, C., D. D. Do, and D. Nicholson (2013). Condensation and Evaporation in Capillaries with Nonuniform Cross Sections. *Industrial and Engineering Chemistry Research*, **52**(39); 14304–14314

Fitri, E. S., R. Mohadi, N. R. Palapa, S. A. Rachman, and A. Lesbani (2024). Selective Removal of Anionic and Cationic Dyes Using Magnetic Composites. *Science and Technology Indonesia*, **9**(1); 129–136

Gibas, A., A. Baszczuk, I. Jacukowicz-Sobala, A. Ciechanowska, M. Jasiorski, E. Dworniczek, A. Seniuk, and A. Lewińska (2024). H_2O_2-Sensitized Titania with Activity Under Visible Light and in the Dark. *Journal of Environmental Chemical Engineering*, **12**(5); 113975

Gibas, A., M. Winnicki, A. Baszczuk, and M. Jasiorski (2025). Aerosol-Assisted Low-Pressure Cold Spraying of TiO_2 Suspension. *Surface and Coatings Technology*, **496**; 131715

He, Y., N. B. Sutton, H. H. H. Rijnaarts, and A. A. M. Langenhoff (2016). Degradation of Pharmaceuticals in Wastewater Using Immobilized TiO_2 Photocatalysis Under Simulated Solar Irradiation. *Applied Catalysis B: Environmental*, **182**; 132–141

Huang, Y.-S. and H.-W. Liu (2014). Growth Morphologies of Nanostructured Rutile TiO_2. *Journal of Materials Engineering and Performance*, **23**(4); 1240–1246

Irie, H., Y. Watanabe, and K. Hashimoto (2003a). Carbon-Doped Anatase TiO_2 Powders as a Visible-Light Sensitive

Photocatalyst. *Chemistry Letters*, **32**(8); 772–773

Irie, H., Y. Watanabe, and K. Hashimoto (2003b). Nitrogen-Concentration Dependence on Photocatalytic Activity of $TiO_{2-x}N_x$ Powders. *The Journal of Physical Chemistry B*, **107**(23); 5483–5486

Ishigaki, T., Y. Nakada, N. Tarutani, T. Uchikoshi, Y. Tsujimoto, M. Isobe, H. Ogata, C. Zhang, and D. Hao (2020). Enhanced Visible-Light Photocatalytic Activity of Anatase-Rutile Mixed-Phase Nano-Size Powder Given by High-Temperature Heat Treatment. *Royal Society Open Science*, **7**(1); 191539

Jacob, K. A., P. M. Peter, P. E. Jose, C. J. Balakrishnan, and V. J. Thomas (2022). A Simple Method for the Synthesis of Anatase-Rutile Mixed Phase TiO_2 Using a Convenient Precursor and Higher Visible-Light Photocatalytic Activity of Co-Doped TiO_2. *Materials Today: Proceedings*, **49**; 1408–1417

Kacem, M., G. Plantard, M. Brienza, and V. Goetz (2017). Continuous-Flow Aqueous System for Heterogeneous Photocatalytic Disinfection of Gram-Negative *Escherichia coli*. *Industrial & Engineering Chemistry Research*, **56**(51); 15001–15007

Lazar, M., S. Varghese, and S. Nair (2012). Photocatalytic Water Treatment by Titanium Dioxide: Recent Updates. *Catalysts*, **2**(4); 572–601

Lei, Y., Y. Yang, P. Zhang, J. Zhou, J. Wu, K. Li, W. Wang, and L. Chen (2021). Controllable One-Step Synthesis of Mixed-Phase TiO_2 Nanocrystals with Equivalent Anatase/Rutile Ratio for Enhanced Photocatalytic Performance. *Nanomaterials*, **11**(5); 1347

Li, H., X. Shen, Y. Liu, L. Wang, J. Lei, and J. Zhang (2015). Facile Phase Control for Hydrothermal Synthesis of Anatase-Rutile TiO2 with Enhanced Photocatalytic Activity. *Journal of Alloys and Compounds*, **646**; 380–386

Liu, X., Y. Li, D. Deng, N. Chen, X. Xing, and Y. Wang (2016). A One-Step Nonaqueous Sol–Gel Route to Mixed-Phase TiO2 with Enhanced Photocatalytic Degradation of Rhodamine B Under Visible Light. *CrystEngComm*, **18**(11); 1964–1975

Mandari, K. K., B. S. Kwak, A. K. R. Police, and M. Kang (2017). In-Situ Photo-Reduction of Silver Particles and Their SPR Effect in Enhancing the Photocatalytic Water Splitting of Ag_2O/TiO_2 Photocatalysts Under Solar Light Irradiation: A Case Study. *Materials Research Bulletin*, **95**; 515–524

Mardiana, L., N. B. Fajriah, R. Wirawan, T. A. Alaydrus, and S. Rahayu (2026). Functionalization of Titanium Dioxide Nanoparticles in Anatase-Rutile Phases and Quartz Crystal Microbalance for Humidity Sensing Materials. *Science and Technology Indonesia*, **11**(1); 252–260

Murawski, K., T. Manyk, and M. Kopytko (2023). Analysis of Temperature-Dependent Photoluminescence Spectra in Mid-Wavelength Infrared InAs/InAsSb Type-II Superlattice. *Journal of Electronic Materials*, **52**(11); 7089–7094

Pallotti, D. K., L. Passoni, P. Maddalena, F. Di Fonzo, and S. Lettieri (2017). Photoluminescence Mechanisms in Anatase and Rutile TiO_2. *The Journal of Physical Chemistry C*, **121**(16); 9011–9021

Pelaez, M., N. T. Nolan, S. C. Pillai, M. K. Seery, P. Falaras, A. G. Kontos, P. S. M. Dunlop, J. W. J. Hamilton, J. A. Byrne, K. O'Shea, M. H. Entezari, and D. D. Dionysiou (2012). A Review on the Visible Light Active Titanium Dioxide Photocatalysts for Environmental Applications. *Applied Catalysis B: Environmental*, **125**; 331–349

Rajabi, M., S. Shogh, and A. Irajizad (2015). Defect Study of TiO_2 Nanorods Grown by a Hydrothermal Method Through Photoluminescence Spectroscopy. *Journal of Luminescence*, **157**; 235–242

Rokade, S. D., D. V. Nandanwar, S. B. Kondawar, P. A. Bramhankar, P. B. Wasnik, and M. S. Bisen (2024). Synthesis and Characterization of Polyaniline/TiO_2 Nanocomposite-Based Ammonia Gas Sensor. *Next Research*, **1**(2); 100065

Sabyrov, K. and R. L. Penn (2016). A Kinetic Model for Two-Step Phase Transformation of Hydrothermally Treated Nanocrystalline Anatase. *CrystEngComm*, **18**(17); 3033–3039

Spada, E. R., E. A. Pereira, M. A. Montanhera, L. H. Morais, R. G. Freitas, R. G. F. Costa, G. B. Soares, C. Ribeiro, and F. R. de Paula (2017). Preparation, Characterization and Application of Phase-Pure Anatase and Rutile TiO_2 Nanoparticles by New Green Route. *Journal of Materials Science: Materials in Electronics*, **28**(22); 16932–16938

Teamsinsungvon, A., C. Ruksakulpiwat, P. Amonpattaratkit, and Y. Ruksakulpiwat (2022). Structural Characterization of Titanium–Silica Oxide Using Synchrotron Radiation X-Ray Absorption Spectroscopy. *Polymers*, **14**(13); 2729

Tovani, C., C. Ferreira, A. Simão, M. Bolean, L. Coppeta, N. Rosato, M. Bottini, P. Ciancaglini, and A. Ramos (2020). Characterization of the in Vitro Osteogenic Response to Submicron TiO_2 Particles of Varying Structure and Crystallinity. *ACS Omega*, **5**(20); 11491–11501

Vaez, M., S. Alijani, M. Omidkhah, and A. Zarringhalam Moghaddam (2018). Synthesis, Characterization and Optimization of N-TiO_2/PANI Nanocomposite for Photodegradation of Acid Dye Under Visible Light. *Polymer Composites*, **39**(12); 4605–4616

Wahyuni, S., S. Kadarwati, M. Alauhdin, S. Priatmoko, N. H. Sani, R. Prasetyo, and I. A. Putri (2026). Enhanced Visible-Light Photocatalytic Degradation of Methylene Blue Using TiO_2/g-C_3N_4 Composites Synthesized via Co-Calcination. *Results in Chemistry*, **24**; 103230

Wahyuni, S., I. Kartini, and S. Kadarwati (2024). The Properties and Activity of TiO_2-Based Nanorods as an Anti-Fouling Agent and a Photocatalyst. *Bulletin of Chemical Reaction Engineering and Catalysis*, **19**(1); 47–60

Wahyuni, S., E. S. Kunarti, R. T. Swasono, and I. Kartini (2018). Characterization and Photocatalytic Activity of TiO_2(Rod)-SiO_2-Polyaniline Nanocomposite. *Indonesian Journal of Chemistry*, **18**(2); 321–330

Wang, J., D. N. Tafen, J. P. Lewis, Z. Hong, A. Manivannan, M. Zhi, M. Li, and N. Wu (2009). Origin of Photocatalytic Activity of Nitrogen-Doped TiO_2 Nanobelts. *Journal of the American Chemical Society*, **131**(34); 12290–12297

Wang, K., Y. Zhuo, J. Chen, D. Gao, Y. Ren, C. Wang, and Z. Qi (2020). Crystalline Phase Regulation of Anatase-Rutile TiO_2 for the Enhancement of Photocatalytic Activity. *RSC Advances*, **10**(71); 43592–43598

Wu, C.-Y., K.-J. Tu, Y.-S. Lo, Y. L. Pang, and C.-H. Wu (2016). Alkaline Hydrogen Peroxide Treatment for TiO_2 Nanoparticles with Superior Water-Dispersibility and Visible-Light Photocatalytic Activity. *Materials Chemistry and Physics*, **181**; 82–89

Xie, Z., Q. Meng, Y. Hu, Y. Tang, K. Wang, Y. Zhang, X. Yu, K. Zhao, and C. Xu (2024). Amorphous Titanium Dioxide with Abundant Defects Induced by Incorporation of Silicon Dioxide: A Potential Non-Radical Activator of Hydrogen Peroxide. *Journal of Colloid and Interface Science*, **653**; 1006–1017

Yaemsunthorn, K., M. Kobielusz, and W. Macyk (2021). TiO_2 with Tunable Anatase-to-Rutile Nanoparticles Ratios: How Does the Photoactivity Depend on the Phase Composition and the Nature of Photocatalytic Reaction? *ACS Applied Nano Materials*, **4**(1); 633–643

Yu, J. C., J. Yu, W. Ho, Z. Jiang, and L. Zhang (2002). Effects of F-Doping on the Photocatalytic Activity and Microstructures of Nanocrystalline TiO_2 Powders. *Chemistry of Materials*, **14**(9); 3808–3816

Zhang, C., Y. Zhou, Y. Li, X. Yang, K. Liu, A. Ayyub, K. H. Lim, W. Zheng, M. Xu, W. Yang, and S. Kawi (2025). Polyol-Solid Surface/Interface Transesterification Strategy to Construct Precise Anatase/Rutile TiO_2 Hetero-Phase Junctions Towards Enhanced Photocatalytic Performance. *Energy Materials*, *5*(9); 1–14

Zhang, J., L. Li, D. Liu, J. Zhang, Y. Hao, and W. Zhang (2015). Multi-Layer and Open Three-Dimensionally Ordered Macroporous TiO_2–ZrO_2 Composite: Diversified Design and the Comparison of Multiple Mode Photocatalytic Performance. *Materials & Design*, **86**; 818–828

Zhang, J., S. Yan, L. Fu, F. Wang, M. Yuan, G. Luo, Q. Xu, X. Wang, and C. Li (2011). Photocatalytic Degradation of Rhodamine B on Anatase, Rutile, and Brookite TiO2. *Chinese Journal of Catalysis*, **32**(6–8); 983–991

Zhang, J., P. Zhou, J. Liu, and J. Yu (2014). New Understanding of the Difference of Photocatalytic Activity Among Anatase, Rutile and Brookite TiO_2. *Physical Chemistry Chemical Physics*, **16**(38); 20382–20386

Zhang, Y., J. Chen, and X. Li (2010). Preparation and Photocatalytic Performance of Anatase/Rutile Mixed-Phase TiO_2 Nanotubes. *Catalysis Letters*, **139**(3–4); 129–133

Zhao, Z., J. Sun, G. Zhang, and L. Bai (2015). The Study of Microstructure, Optical and Photocatalytic Properties of Nanoparticles (NPs)-Cu/TiO_2 Films Deposited by Magnetron Sputtering. *Journal of Alloys and Compounds*, **652**; 307–312

Zhou, T., S. Tan, Y. Guo, L. Ma, M. Gan, H. Wang, X. Sun, and H. Wang (2015). A Laminated Spherical Composite Assembled by Alternating Polyaniline and Titania Nanosheets with Enhanced Visible-Light Photocatalytic Activity. *Journal of Alloys and Compounds*, **652**; 358–363

